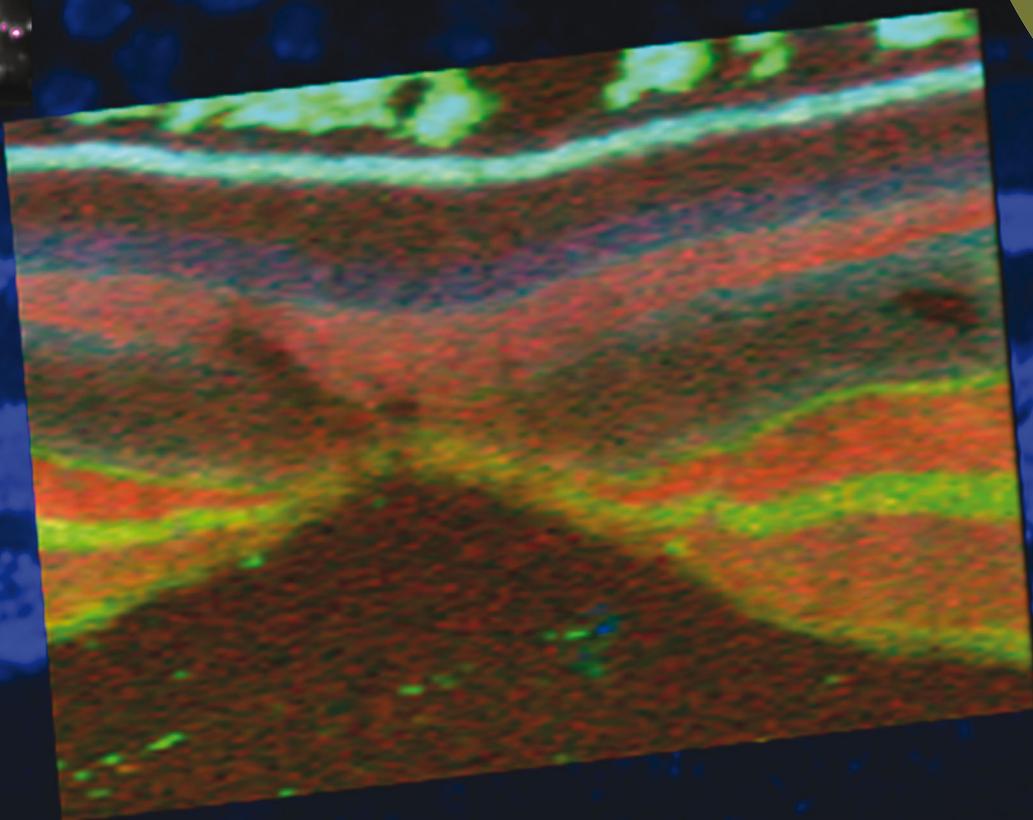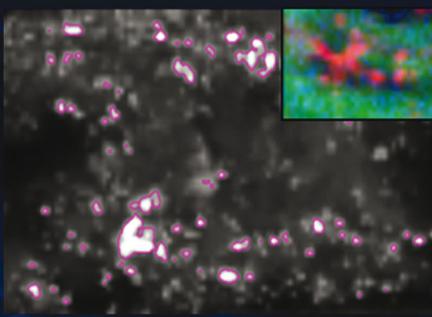# Metallomics

www.rsc.org/metallomics

Indexed in Medline!

ROYAL SOCIETY OF CHEMISTRY

PAPER
Marta Ugarte *et al.*
Iron accumulates in the primate choroid of the eye with aging as revealed with synchrotron X-ray fluorescence microscopy

Metallomics

PAPER

Iron accumulates in the primate choroid of the eye with aging as revealed with synchrotron X-ray fluorescence microscopy

Marta Ugarte,*[ab] Kalotina Geraki[c] and Glen Jeffery[d]

Aging leads to an increase in iron-loaded cellular structures in the choroid of the eye. This study was carried out to determine the distribution and content of iron, zinc and copper in the macular retina, choroid and retrobulbar optic nerve of young (4–5 years, n = 3) and aged (15–16 years, n = 5) male non-human primates, *Macaca fascicularis*, whose ocular anatomy is similar to humans. Thirty μm-thick tissue sections were analysed with synchrotron X-ray fluorescence and stained histologically for iron deposition. Quantitative measurements showed high levels of iron, zinc and copper in the choroid and retinal pigment epithelium in the macular area and arachnoid layer in the retrobulbar optic nerve. In aged animals compared to young ones, there was an increase in iron in the choroid with larger deposits and iron-loaded cellular structures. Iron-accumulation within these cellular structures may contribute to choroidal function impairment in aging and age-related macular degeneration.

Significance to metallomics

Iron-accumulation within cellular structures in the choroid with aging may contribute to reduced choroidal function with aging and age-related macular degeneration. Understanding the mechanisms of iron accumulation and the potential effects will allow us to develop therapeutic measures to prevent visual loss. Blocking hepcidin expression or function may represent an approach to prevent iron retention in cells with high ferroportin expression (such as macrophages). This approach would have advantages over non-specific reduction of iron levels by chelating agents.

Introduction

Iron, zinc and copper are abundant trace elements in the retina.[1,2] They are key structural components of several proteins and cofactors for enzymes. They are involved in many key biological processes including oxygen transportation, DNA synthesis, mitochondrial respiration, myelin synthesis, neurotransmitter synthesis and metabolism.[3] Increasing evidence suggests that zinc and copper also function as signalling molecules in the nervous system being released from synaptic terminals.[4] Dysregulation of iron, zinc and copper homeostases is associated with retinal disease (*e.g.* age-related macular degeneration, AMD).[5–7] In healthy aging, accumulation of iron mainly bound

to ferritin has been shown in the retinal pigment epithelium (RPE) and Bruch's membrane with Perls staining.[8] However, no studies have been carried out in the choroid, which is the major vascular supply to the retina. The choroid contains the highest metal concentrations in the adult eye.[9] Aging is the major risk factor for AMD and the choroid is likely to be vulnerable to effects of metal imbalance and has been implicated in AMD aetiology.

Here, we examine the distribution and concentration of iron, zinc and copper in normally aging non-human primate retina, choroid and optic nerve using micro and nano-beam synchrotron X-ray fluorescence (SXRF) microscopy. We used *Macaca fascicularis*, old world primates with a retina similar to human.[10] Our study constitutes a detailed metallomic map of non-human primate retina, choroid and optic nerve so that the typical changes in metal concentration within these tissues are revealed in normal aging and may be used as a platform for aberrant metal homeostasis. SXRF analysis allows the mapping of total metal content and the alignment of anatomical features with their biological functionality.

[a] Moorfields Eye Hospital NHS Foundation Trust, London EC1V 2PD, UK. E-mail: mugarte@doctors.org.uk

[b] NIHR Biomedical Research Centre, Moorfields Eye hospital and UCL Institute of Ophthalmology, London, UK

[c] I18, Diamond Light Source, Harwell Science and Innovation Campus, Fermi Ave, Didcot, Oxfordshire OX11 0DE, UK

[d] UCL Institute of Ophthalmology, 11-43 Bath St, London EC1V 9EL, UK

Methods

Animals and tissue preparation

All animal procedures were undertaken under local ethical procedures and in line with the UK Home Office regulations [Animals (Scientific Procedures) Act 1986] and the tenets of the ARVO statement on the Use of Animals in Ophthalmic and Vision Research.[11] Trace element contamination was minimised by using analytical grade reagents and handling samples in clean environments with titanium tools. Cynomolgous long-tailed monkeys (*Macaca fascicularis*) were used in the study. Macaques are genetically very similar to humans with analogous neurological, reproductive and immunological systems. Animals were provided with a commercially available primate diet and water ad libitum. All macaques were clinically healthy during the study period. They did not receive any trace element supplements or blood transfusions. Unnatural constraint (laboratory rearing *versus* free ranging) is unlikely to have affected trace element metabolism. Three young (4–5 years) and 5 aged (15–16 years) male animals were sedated with 0.1 mg kg^{-1} Dormitol and 200 mg kg^{-1} Ketamine intramuscularly in the morning after their usual 12 h:12 h light dark cycle. Animals were then bled out, humanely killed with 2.5 ml Nembutal (50 mg sodium pentobarbital per ml) intracardial injection and their eyes removed. Primary animal use was for purpose of other (*i.e.* vaccine testing) than the experiments described here. After dissecting the cornea, iris and lens, the remaining of the eyeballs were fixed in 4% paraformaldehyde for less than 48 h and cryo-preserved in 25% sucrose before embedding in optimum cutting temperature Tissue-Tek® compound. Thirty μm-thick sections of retina and choroid from the macular region (Fig. 1) and retrobulbar optic nerve were cut with a cryostat, placed on thin film and allowed to air dry. Within the following 36 h, the tissue samples were imaged at the synchrotron Diamond Light Source (Harwell Science and Innovation Campus, UK).[12]

Synchrotron X-ray fluorescence (SXRF) microscopy

The distribution of total iron, zinc and copper was mapped in air at room temperature using SXRF microscopy at two beamlines of the Diamond Light Source. Cryosections were mounted on thin

Fig. 1 Localisation of the tissues in the macular area for which scans were obtained. (1) Position of the fovea centralis, the central pit composed of densely packed cones, (2) full thickness retina from the macular region (within 1 mm from the centre of the fovea) and (3) choroid. Scale bar 50 μm.

film (Ultralene) used for X-ray trace element analysis as it does not contain any metals in detectable levels. Different section thicknesses were prepared to test signal *versus* spatial resolution. Thirty μm was found to be an optimal thickness. I18,[13] the Microfocus Spectroscopy beamline, was used first to map the sections at micron level resolution. B16,[14] the Test beamline, was then employed to investigate selected regions with sub-micron resolution. Both beamlines use Kirkpatrick Baez mirrors for focusing the X-ray beam. The energy used on I18 to excite the elements of interest was 11 keV while on B16 it was 17 keV. For all measurements, silicon drift detectors were used (six-element SGX on I18, four-element Vortex on B16). Apart from the trace elements of interest, phosphorus and sulphur were also detected but with much lower sensitivity.

After visual inspection of each eye section with the on-line camera, regions were selected for mapping. For the first round of measurements on I18 a beam of 5×2 μm^2 ($H \times V$) was used. This set of measurements identified the choroid as the main target of interest but also suggested that the structures identified for further study were quite small. A second set of measurements took place on I18 with the beam focused to 2×2 μm^2 concentrating only on the choroid. Approximate areas of 200×100 μm^2 were mapped on each sample. The shape and size of the structures with high iron signal were further investigated on B16 with a resolution of 0.5×0.5 μm^2.

Processing of the raw data involved peak fitting and background removal. Semi-quantitative calculation of the trace element concentrations was carried out by measuring a reference material (AXO, Dresden GmbH) in the same conditions as the samples. The reference material is composed of nm-thick layers of metals with known numbers of atoms per unit area. The software package used for the analysis was PyMca[15] in which both the reference material and the sample are modelled in terms of main composition, density and thickness. The net peak areas from the sample spectra are translated into concentrations resulting in elemental maps in units of ppm (μg g^{-1} dry weight). The elemental distribution maps were created by recording the spatially resolved intensities of characteristic photons on a 2-dimensional grid of equally sized pixels. Each pixel represents a defined finite sized area in a specific location in the specimen. The characteristic photons from each element detected at each pixel were converted to concentration values therefore the contrast of the maps represents concentration gradients. The maps were then imported as tiff images in ImageJ[16] for further statistical analysis. A number of regions of interest (ROI) representing individual retinal layers were defined for each metal and average ROI values (mean ± standard deviation) calculated as a parameter for comparison. The profile of a single pixel line (manually defined from the outer to the inner part of the retina) from each map was also evaluated. These show specific layers where individual trace elements were more abundant. The difficulties in measuring and quantifying sulphur and phosphorus resulted in underestimated concentrations for the two elements.

Perl's staining

For each animal sample, 10 μm-thick sections from the macular area were cut serially (alternating with the 30 μm thick sections for SXRF analysis) with a cryostat. Sections 2, 4 and 6 were
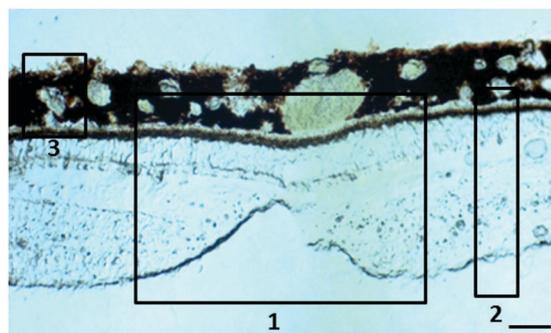
stained for ferric iron (Fe^{3+}) with Perl's method[17] using a freshly prepared incubating solution containing 2% potassium ferrocyanide, 2% hydrochloric acid (1 : 1). This staining method was chosen to correlate the SXRF findings independently. Non-heme iron (predominantly Fe^{3+} bound to ferritin or transferrin and very small amounts bound to organic bases, enzymes, iron sulphur proteins and nucleotides) can be visualised with Perl's iron stain, in which soluble ferrocyanide reacts with the tissue Fe^{3+} to form crystals that make insoluble Prussian blue dye.

Estimates of the numbers of iron-loaded cellular structures

To investigate the prevalence and size of the iron-loaded structures and how these vary between the young and aged animals (n = 3 and 5 respectively), we performed particle analysis on the $200 \times 100~\mu m^2$ SXRF maps in ImageJ. We used a threshold based approach to analyse the regions above a pre-set intensity. Higher intensity corresponds with the presence of a particular structure or substance with accumulation of a specific trace element. A threshold of 1000 ppm was applied and structures above this were identified, counted and their dimensions were extracted. For statistical analysis, the unpaired Student t test was used. The differences of $p < 0.05$ were considered significant.

Results and discussion

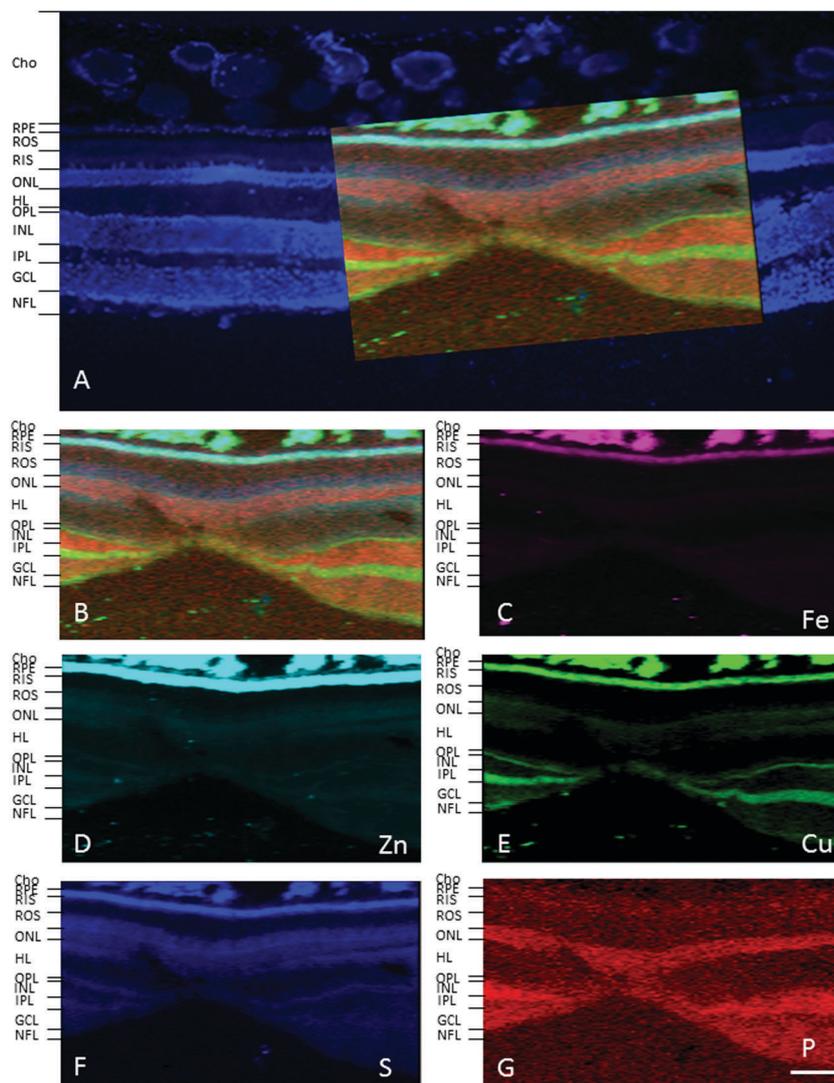In the adult young primate, the choroid and RPE were shown to contain high levels of iron, zinc and copper (Fig. 2, 3

Fig. 2 Synchrotron X-ray fluorescence (SXRF) maps for selected elements in the fovea. (A) Formalin-fixed 30 μm section stained with 4',6-diamidino-2-phenylindole, DAPI, to identify the retinal layers containing cell bodies (*i.e.* RPE, ONL, INL, GCL). (B) Merged map indicating P (red), S (blue), Cu (green). Single element maps for Fe (C), Zn (D), Cu (E), S (F) and P (G). The choroid and RPE contain high levels of iron, zinc and copper. Within the neuroretina, copper was localised in both plexiform layers (*i.e.* OPL and IPL) and NFL. Abbreviations: cho, choroid; GCL, ganglion cell layer; INL, inner nuclear layer; IPL, inner plexiform layer; NFL, nerve fibre layer; ONL, outer nuclear layer; OPL, outer plexiform layer; RIS, photoreceptor inner segments; ROS, photoreceptor outer segments. Scale bar 50 μm.

and Tables 1, 2). In the choroid, we measured (mean ± SD) 350 ± 178.8 ppm iron, 312 ± 209 ppm zinc and 22.6 ± 9.6 ppm copper. In the RPE, 152 ± 26.5 ppm iron, 110 ± 89 ppm zinc and 9 ± 3 ppm copper. In the neuroretina, copper was localised in the outer plexiform layer (OPL) (7.4 ± 6 ppm), inner plexiform layer (IPL) (9 ± 3.2 ppm); and nerve fibre layer (NFL) (6 ± 2.2 ppm) (Fig. 3). In contrast, the neuroretina was virtually devoid of iron and zinc.
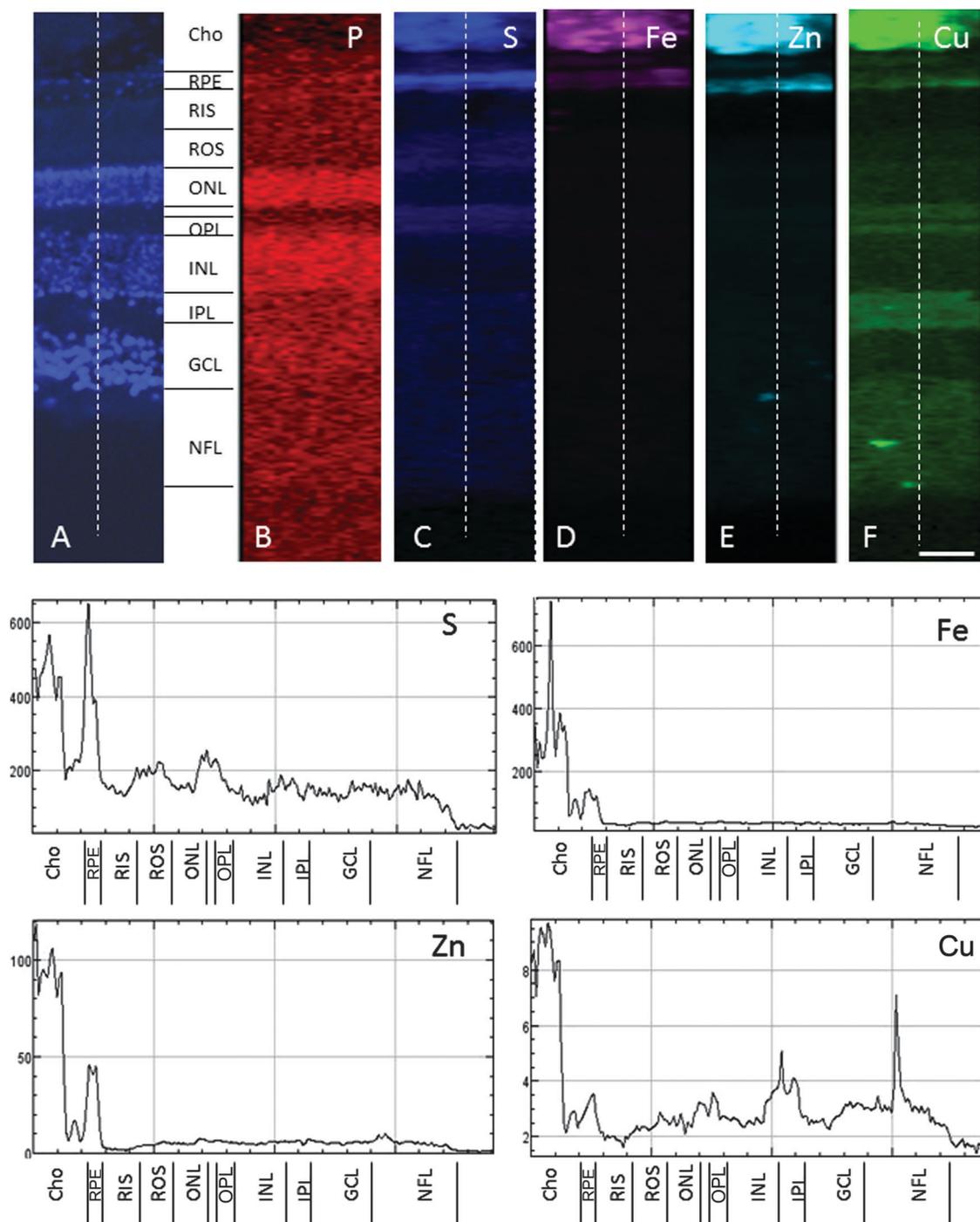

Fig. 3 SXRF maps of full-thickness retina in the macula. (A) Formalin-fixed 30 μm section stained with DAPI to identify the retinal layers containing cell bodies. Single element maps for P (B), S (C), Fe (D), Zn (E) and Cu (F). The choroid and RPE contain high levels of iron, zinc and copper. Within the neuroretina, copper was associated with the synaptic layers (*i.e.* OPL and IPL) and NFL. These regions were virtually devoid of iron and zinc. The dashed lines on the maps indicate the position of the profiles shown below. The peaks with the highest concentrations of iron, zinc and copper correspond with the choroid and RPE. Copper peaks in the neuroretina were found in the OPL, IPL and NFL. Abbreviations as in Fig. 2. The concentrations in each layer can be found in Table 1. Scale bar 50 μm.

Table 1 Comparison of the concentrations (mean ± SD) of trace elements in different retinal layers (ROI) in the macular areas in young (n = 3) and aged (n = 5) *Macaca fascicularis*

Young	Fe	Zn	Cu	P	S
Choroid	350.9 ± 178.8	312.1 ± 209	22.6 ± 9.6	130.7 ± 42	553 ± 149
RPE	152 ± 26.5	110 ± 89	9 ± 3	225 ± 152	253 ± 93
ROS	28 ± 1.7	6 ± 1.2	3 ± 0.4	135 ± 17	143 ± 55
RIS	27 ± 2.4	7 ± 1	3 ± 0.2	153 ± 15	215 ± 36
ONL	33 ± 3.2	7 ± 1.5	4 ± 1.3	235 ± 33.5	168 ± 36.3
OPL	29 ± 1	8.4 ± 3	7.4 ± 6	132 ± 14.1	246 ± 81.5
INL	40 ± 9.3	7.5 ± 2.8	4 ± 0.4	255 ± 51.6	171 ± 51
IPL	37 ± 5	8.5 ± 2.3	9 ± 3.2	202 ± 26	213 ± 59.7
GCL	42 ± 10	9.1 ± 4.1	4.7 ± 1.1	242 ± 58.2	209 ± 80
NFL	33 ± 8	7.6 ± 4.5	6 ± 2.2	172 ± 17.6	159 ± 40

Aged	Fe	Zn	Cu	P	S
Choroid	347.9 ± 159.7	171.5 ± 93.5	16.5 ± 5.5	49 ± 16	501 ± 118
RPE	161.2 ± 41	155 ± 86.4	5.3 ± 2.2	142.5 ± 27.7	471.3 ± 137.7
ROS	41.7 ± 21.6	13.8 ± 18.1	2.1 ± 0.4	133 ± 19.5	167.8 ± 41
RIS	32.6 ± 3.6	6.9 ± 1	2.9 ± 1.6	151.6 ± 15.6	304.2 ± 41.6
ONL	36.5 ± 6.3	7.4 ± 3.7	2.9 ± 0.8	234.5 ± 68.2	216.7 ± 2.5
OPL	30.2 ± 4.5	7 ± 3.9	3.3 ± 1	142.2 ± 23.7	226 ± 68
INL	34.1 ± 2.4	6.1 ± 1.3	2.9 ± 0.7	239 ± 64.5	163.2 ± 20.8
IPL	34.8 ± 1.8	6.7 ± 1.4	3.7 ± 1.2	179.9 ± 22.5	175.7 ± 32.7
GCL	34.9 ± 2.3	6.1 ± 1.3	3.5 ± 0.3	198 ± 46.1	175.1 ± 31.5
NFL	34.1 ± 3.6	7.7 ± 4.2	4.2 ± 1.4	196.5 ± 50.1	154.1 ± 25.9

Table 2 Range of concentrations (ppm) of iron, zinc and copper in individual young and aged non-human primate choroid

	Iron	Zinc	Copper
Young 1	48–1587	36–807	4–28
Young 2	41–1334	10–448	12–61
Young 3	34–1391	16–777	24–63
Aged 1	18–2999	2–574	5–24
Aged 2	109–3752	44–803	15–61
Aged 3	79–3226	34–574	4–34
Aged 4	30–3079	10–759	15–21

In the adult young choroid, iron was detected in hotspots with concentration levels of up to 1391 ppm (Fig. 4, 5 and Table 3). As can be appreciated by the contrast in the maps presented, intra-tissue regional heterogeneity associated with variations in tissue architecture resulted in a wide range of pixel intensity values in the image brightness (*i.e.* corresponding to element concentrations) at this high level of spatial resolution. The levels quoted in the corresponding tables (minimum–maximum pixel intensity) demonstrate local spatial variation in element concentration. We used a threshold of 1000 ppm of iron (Tables 3 and 4) and focused on highly enriched areas. The anatomical features of these iron hot spots were further characterized by higher resolution measurements (B16). As seen in Fig. 6 and 7, hotspots included ovoid and branched cellular structures with size up to 20 μm in diameter, whose cytoplasm seemed to be completely filled with iron. In choroidal vessels (*i.e.* blood or lymphatic), iron-positive ovoid cellular structures (2–4 μm in diameter) could be seen in the lumen.

When comparing the distribution and concentrations of trace elements in adult young (4–5 years) and aged (15–16 years) monkeys, no differences were detected in iron, zinc or copper in the RPE or neuroretina. By contrast, in the aging choroid,

the overall concentration of iron was higher while that of copper was lower (Fig. 4). Moreover, significantly more and larger hotspots with higher fluorescence intensities occurred with aging (Fig. 4 and 5). In areas of 200×100 μm^2 a total of 4–8 iron-loaded structures were found in the young samples compared to 16–93 in the aged animals ($p < 0.001$, unpaired Student's *t*-test) (Fig. 4–7 and Table 3). The branched hotspots in the aged choroid had a maximum diameter of 22 μm compared to 13 μm in the young choroid. The higher intensity of the iron signal in the hotspots (with concentrations up to 3752 ppm) with aging, suggests accumulation of iron in these cellular structures. Iron hotspots could be seen both in the inner and outer choroid. A few clusters of enlarged ovoid cellular structures with intense iron signal were found within the vessels and stroma. In some regions, hotspots surrounded vessels suggesting a vascular origin. We used blood measurements from the central retinal artery and vein in the optic nerve as a reference for iron values in blood. In spite of the animals being bled out, these vessels still contained significant blood volumes. The iron concentrations in the hotspots in the aged choroid were 3–4 fold higher than in blood. The iron concentration differences between hotspots in young and aged animals were up to 2-fold.

The enlarged iron-loaded cellular structures in the aged choroid have low amounts of zinc (Fig. 7). This suggests an alteration of both the homeostasis of iron and zinc in these cellular structures. The Perl's staining pattern in parallel sections demonstrated iron (mainly bound to ferritin) accumulated in some of these cellular structures (Fig. 6).

In the retrobulbar optic nerve, the highest concentration of iron, zinc and copper was found in the arachnoid layer (Fig. 8). This meningeal layer is continuous with the choroid at the head of the optic nerve and ensheaths the retrobulbar nerve between the pia and dura mater. The range of concentrations measured
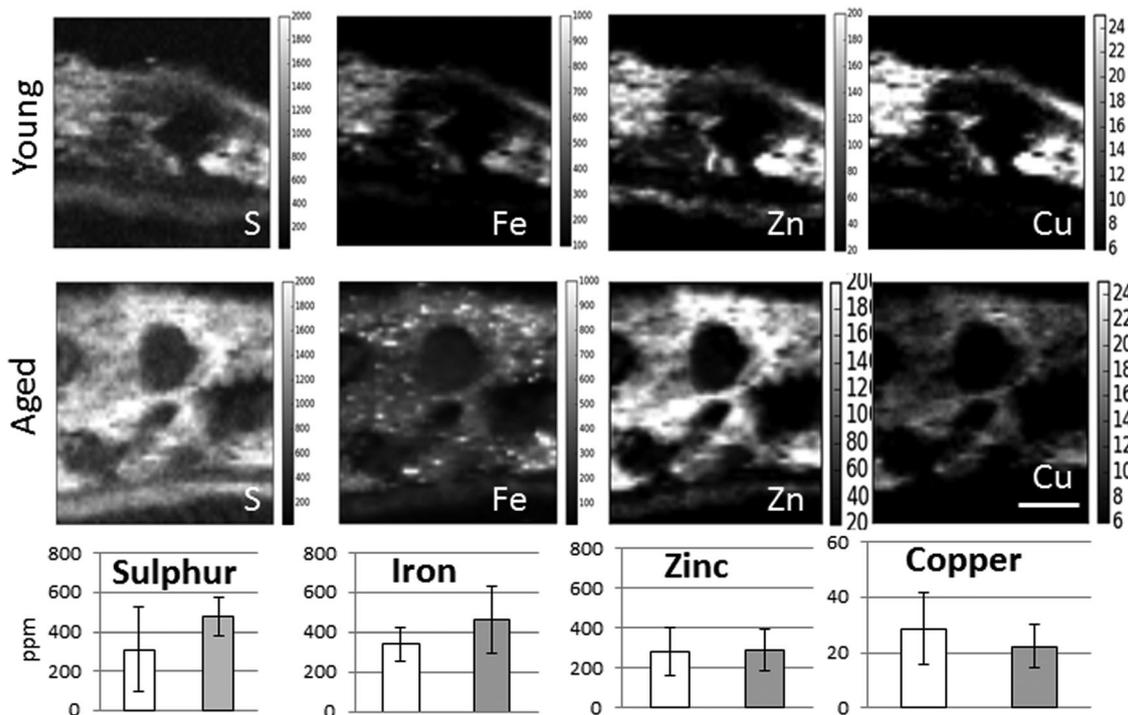
Fig. 4 Comparison of the distribution and content of sulphur, iron, zinc and copper in the choroid of adult young (4 years) and aged (15 years) *Macaca fascicularis*. The number of iron hot spots increases with age while the overall copper concentration decreases. The distribution of zinc is similar in young and aged animals. The hot spots with a high iron signal vary in size and are evenly distributed in the inner and outer choroid. Scale bar 50 μm.
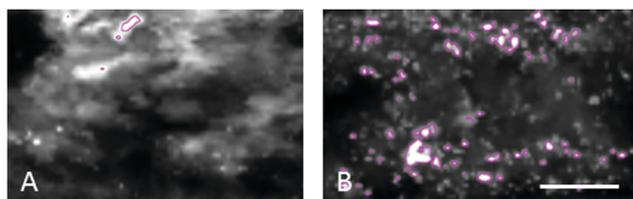

Fig. 5 The number of iron-loaded structures in the choroid of non-human primates increases with age. (A) Young animals were found to have 4–8 structures with >1000 iron ppm per 200×100 μm² area compared to (B) 16–93 in the same area of aged animals. The size of these structures was measured as 2–13 μm in young animals and up to 22 μm in aged. Scale bar 50 μm.

in the arachnoid layer were 45–547 ppm iron, 6–293 ppm zinc and 2.6–25 ppm copper (Table 5). The satellite cells (*e.g.* oligodendrocytes) found in the optic nerve fibres contain levels

Table 4 Iron, zinc and copper content in ppm (mean ± SD) (ranges) in iron-rich hotspots in young and aged choroid. Numbers in left column show cellular structures from Fig. 7

	Iron	Zinc	Copper
2	924 (237–2731)	110 (87–146)	16 (11–23)
5	1508 (452–3272)	40 (31–51)	12 (10–14)
6	941 (456–2061)	48 (39–61)	14 (11–17)
7	809 (185–1406)	75 (59–90)	4 (7–17)

of iron ranging between 55–138 ppm. Within the blood clots in the central retinal vein and artery the concentration ranges for iron, zinc and copper were 37–1097 ppm, 4–64 ppm and 1.8–6.4 ppm, respectively.

Here, we show high levels of iron, zinc and copper in the choroid, RPE and arachnoid layer of the retrobulbar optic nerve. Choroidal iron levels increased with age while those

Table 3 Details of iron-rich hot spots in young and aged choroid

	Number of hotspots with Fe >1000 ppm	Hotspots diameter (μm)	Range of Fe ppm in hotspots[a]	Range of Zn ppm in Fe HS	Range of Cu ppm in Fe HS
Young 1	4	<3	1007–1587	278–491	14–19
Young 2	8	<12	1023–1334	171–420	27–58
Young 3	4	<13	1005–1391	369–509	42–60
Aged 1	16	<21	1015–2999	38–349	6–21
Aged 2	75	<18	1005–3752	63–586	9–51
Aged 3	81	<22	1002–3226	69–505	6–33
Aged 4	93	<17	1003–3079	179–664	13–42

[a] Comparison of the values in young *vs.* aged showed $p < 0.001$ (Student's *t* test).
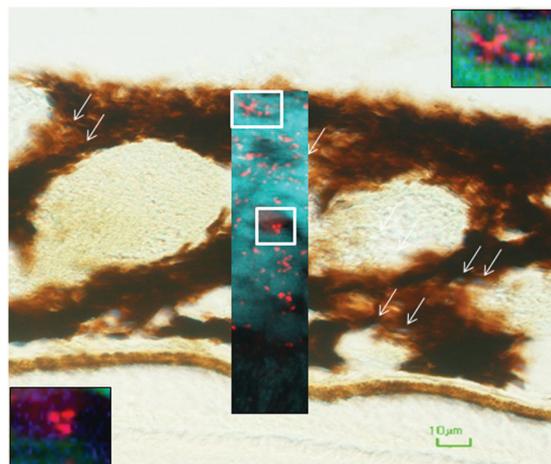
Fig. 6 Iron-loaded structures in the choroid of the macular region of aged non-human primate. Choroidal section stained with Perl's technique identified ferritin-containing granular areas. Overlaid SXRF high-resolution scan shows iron-laden structures some with stellate appearance (top right inset), whereas others had oval-round appearance (bottom left). Scale bar 10 μm.

of copper decreased. These changes are likely to be due to a combination of direct displacement from binding sites and indirectly by stimulating export. Interrelationships between iron, zinc and copper metabolism are well known. Supporting this observation, a 2–3 fold increase in RPE/choroid iron levels has been noticed previously in aged (16–19 month old) compared to young adult (2–6 month old) mice using chromogen-based or atomic absorption spectrophotometry.[18] Iron increase in other tissues with age constitutes further supporting evidence.[19,20] Choroidal iron-loaded cellular structures increased in number, size and iron content. The overall iron concentration in the aging choroid was not significantly higher than in the young. This may be due to the small volume of these cells compared to the total choroid and the small number of subjects.

The neuroretina was virtually devoid of zinc and iron. The loosely bound fraction of these trace elements might have leached out of the tissue into the fixation and cryoprotection solutions.[21,22] In contrast, there appeared to be little, if any, loss of neuroretinal copper, or iron, zinc and copper from the choroid.
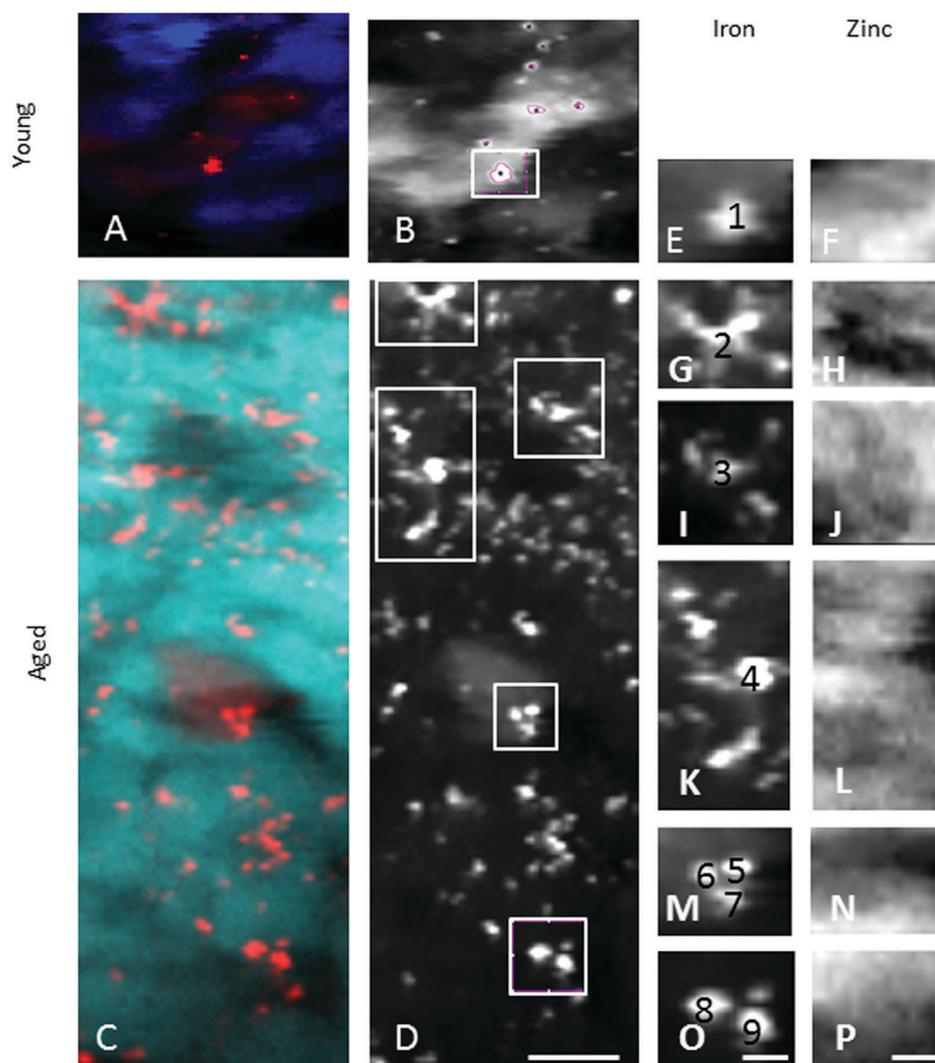

Fig. 7 Iron-rich cellular structures showed low content of zinc suggesting dysregulation of both iron and zinc homeostases in these cellular structures.
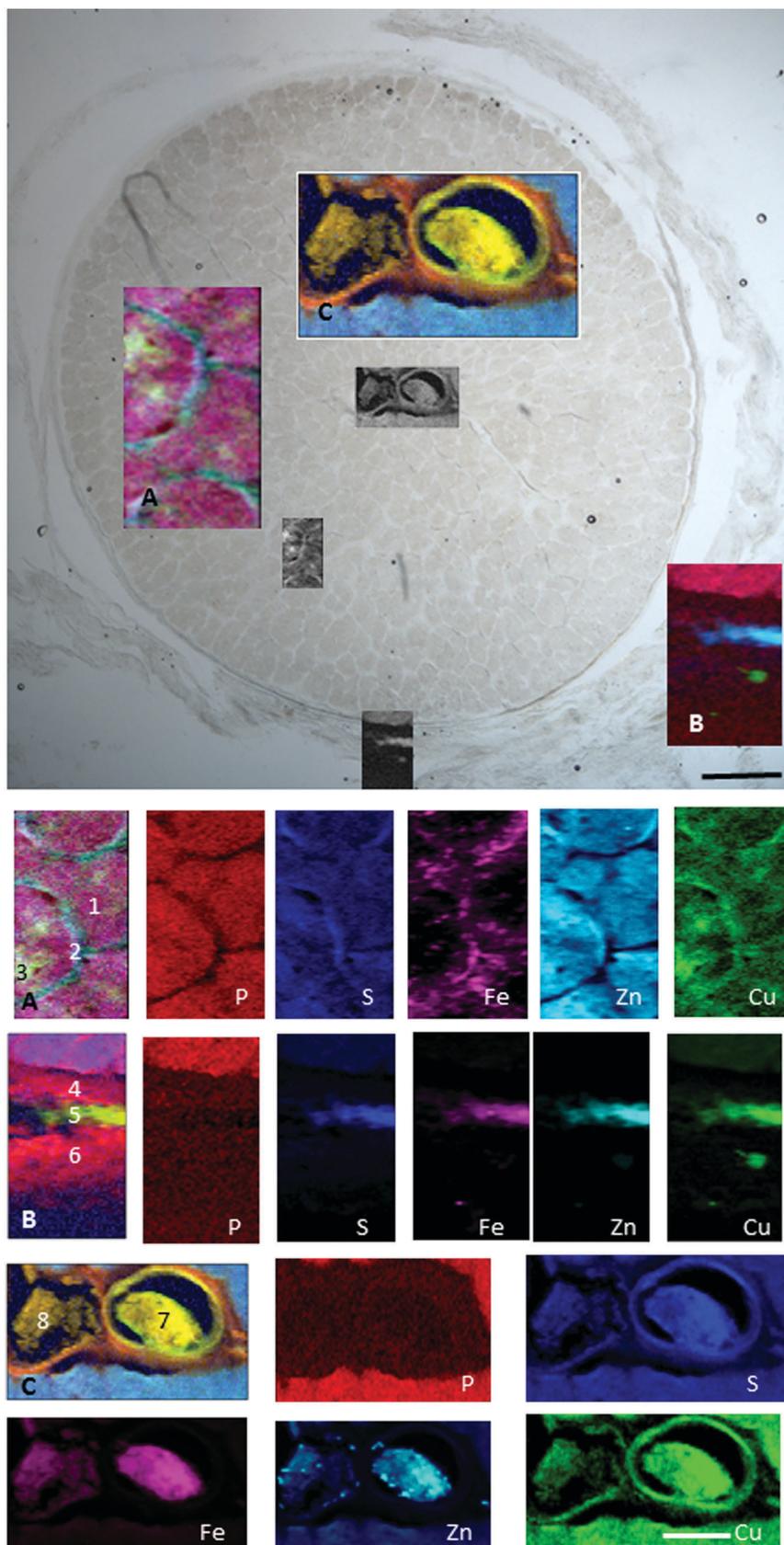
Fig. 8   Retrobulbar (myelinated) optic nerve section. (A) Axons (1), glia (2) and satellite cells (3). (B) Pia (4), arachnoid (5) and dura matter (6). (C) Central retinal artery (7) and vein (8). Maps show trace element distribution. The concentrations of individual elements in different areas can be found in Table 5. Scale bars 100 µm and 50 µm.

Table 5 Iron, zinc, copper, phosphorus and sulphur concentration (ppm) (ranges) in different structures in the optic nerve

		Fe	Zn	Cu	P	S
1	ON axons	54 (37–95)	14 (12–16)	3 (2.5–3.6)	288 (206–365)	289 (249–341)
2	Pial septa	64 (50–92)	15 (9–19)	3.4 (2.8–3.9)	265 (155–371)	344 (251–399)
3	Satellite cells	84 (55–138)	12 (8–16)	3 (2.7–3.5)	255 (137–356)	286 (229–345)
4	Pia	31 (20–54)	3 (1.2–13)	2.3 (1.4–3.2)	115 (49–231)	129 (67–195)
5	Arachnoid	256 (45–547)	155 (6–293)	13.5 (2.6–25)	80 (14–154)	576 (180–974)
6	Dura	32 (18–106)	4 (1–47)	2.7 (1.1–15.8)	105 (45–181)	129 (53–237)
7	Blood clot in CRA	799 (37–1097)	30 (4–64)	4.4 (1.8–6.4)	114 (51–258)	471 (58–669)
8	Blood clot in CRV	480 (111–698)	21 (5–42)	3.4 (2.2–4.2)	119 (50–202)	308 (95–453)

Comparison of our data with previous estimations shows similar choroidal zinc and copper concentrations to unfixed human samples using ICPMS.[7] Similar RPE iron, zinc and copper levels to those measured in unfixed rat sections with particle induced X-ray emission.[1] Lower iron and zinc in the neuroretina but comparable copper levels to unfixed rat sections.[2] It seems reasonable to interpret that our maps represent trace metals tightly bound to proteins and/or sequestered within cytosolic organelles.

To confirm the changes observed were true alterations in iron rather than the consequence of age-related decrease in tissue mass or irregular sample thickness, we analysed the distribution of elements representative of cellularity (i.e. sulphur and phosphorus). There were no significant differences in the concentrations of sulphur of phosphorus between young and aged samples. It is unlikely that the increase in iron observed is the result of increased melanin as zinc and copper, which also bind to it,[23] were not increased. The intensity of non-heme iron staining by Perl's method was moderate in these cellular structures compared to the intense X-ray fluorescence signal, suggesting the presence of heme- and non-heme-bound iron.

The choroidal stroma (extravascular tissue) contains collagen and elastic fibres, together with fibroblasts, melanocytes, non-vascular smooth muscle cells, mast cells, dendritic cells, macrophages and lymphocytes.[24] Based on the morphology (i.e. size, ramification processes), location and relationship with vessels, the most likely candidates of the iron-rich cellular structures are macrophages or dendritic cells.[25] It is possible that with age, iron leaving the plasma is internalised and deposited within certain cellular structures (e.g. macrophages) and due to disruption of iron-complexes digestion, iron transport and/or export accumulates within them (Fig. 9).

Unlike other cells, which take up iron in the form of diferric-transferrin, macrophages phagocytose damaged or senescent erythrocytes, and digest them to extract heme. Upon degradation of heme by heme oxygenase 1, iron is released and exported by the divalent metal transporter 1 to the cytoplasm, delivered for storage in ferritin or exported via the membrane transporter, ferroportin. The release of iron from macrophages is regulated by the interaction of the hepatic protein hepcidin with ferroportin and requires the copper-containing ferroxidase, ceruloplasmin. In this context, mice with hepcidin-resistant ferroportin have been shown to accumulate iron in the retina.[26] Humans with aceruloplasminemia develop RPE iron overload.[27] These mechanisms may also be disrupted with age.

Iron has been shown to accumulate in different tissues (e.g. brain) as a consequence of normal aging (i.e. the continuous
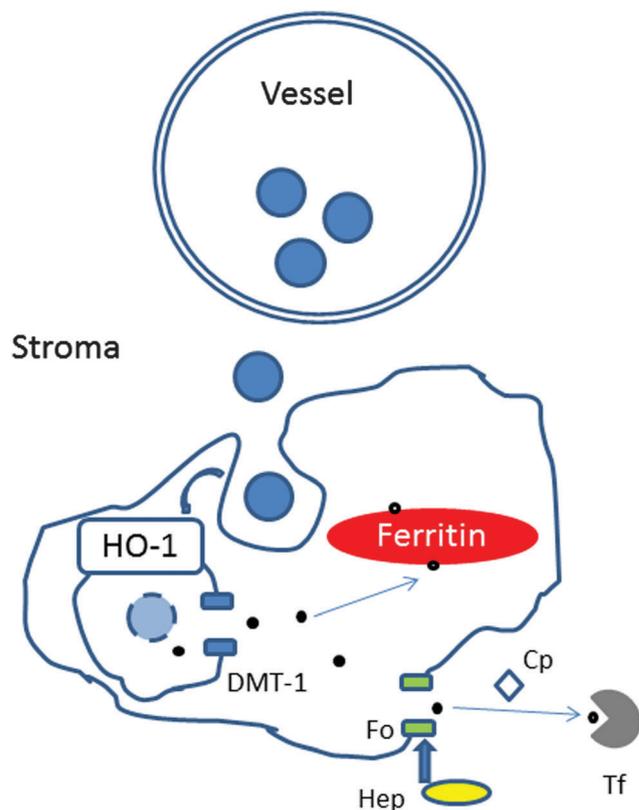

Fig. 9 Schematic representation showing possible mechanisms of iron accumulation in cellular structures in the choroid with age. Upon leaving the choroidal vessel (e.g. within haemoglobin in erythrocyte), iron is internalised by phagocytosis by macrophages. Within the phagosome, heme groups from haemoglobin would be digested by Heme oxygenase 1 (HO-1) to release iron (Fe^{2+}), which is exported to the cytoplasm by Divalent metal transporter 1 (DMT-1). Within the cytoplasm, Fe^{2+} could be delivered for storage in ferritin (as Fe^{3+}) or exported via the membrane transporter ferroportin (Fo). The hepatic protein, hepcidin (Hep), regulates the release of iron by ferroportin. The ferroxidase, ceruloplasmin, is required for iron transport by ferroportin by converting Fe^{2+} to Fe^{3+} form, which can be loaded on to transferrin. We propose that in the aging choroid the digestion of heme by HO-1, the transport of iron by DMT-1 or ferroportin might be reduced resulting in iron accumulation within the macrophages in the stroma.

process of natural change from adulthood without disease). The determinants of iron deposition are not well elucidated. One of the potential reasons is primary iron excess, which stimulates hepcidin expression that blunts ferroportin activity resulting in intracellular iron–ferritin accumulation. Aging affects the cells of

every major organ in the body. Iron accumulation in choroidal cells with aging is likely to determine local interactions between iron-loaded cells and inflammatory cells. This may lead to direct inflammation and choroidal and retinal injury with time.

We propose iron-accumulation within these cellular structures is associated with promotion of oxidative stress,[28] inflammation and membrane attack complex formation, as suggested by brain studies,[29] may contribute to reduced choroidal function with aging. Membrane attack complex formation, the terminal process of complement activation, which can cause cell death, has been shown to increase in the inner choroid during normal aging and especially in age-related macular degeneration.[30]

Conclusion

Synchrotron X-ray fluorescence showed the presence of iron, zinc and copper in high amounts in the choroid, RPE and arachnoid layer of the retrobulbar optic nerve. Iron levels increased with age in the choroid higher number of cellular structures loaded with iron.

List of abbreviations

AMD	Age related macular degeneration
DAPI	4′,6-diamidino-2-phenylindole
DMT-1	Divalent metal transporter 1
GCL	Ganglion cell layer
HO-1	Heme oxygenase 1
INL	Inner nuclear layer
IPL	Inner plexiform layer
NFL	Nerve fibre layer
ONL	Outer nuclear layer
OPL	Outer plexiform layer
ROI	Regions of interest
RPE	Retinal pigment epithelium
SXRF	Synchrotron X ray fluorescence

Acknowledgements

References

1 M. Ugarte, G. M. Grime and N. N. Osborne, *Metallomics*, 2014, **6**, 274–278.

2 M. Ugarte, N. N. Osborne, L. A. Brown and P. N. Bishop, *Surv. Ophthalmol.*, 2013, **58**, 585–609.

3 A. R. White, K. M. Kanninen and P. J. Crouch, *Front. Aging Neurosci.*, 2015, **7**, 12.

4 H. Tamano and A. Takeda, *Metallomics*, 2011, **3**, 656–661.

5 X. He, P. Hahn, J. Iacovelli, R. Wong, C. King, R. Bhisitkul, M. Massaro-Giordano and J. L. Dunaief, *Prog. Retinal Eye Res.*, 2007, **26**, 649–673.

6 M. E. Aronow and E. Y. Chew, *Curr. Opin. Ophthalmol.*, 2014, **25**, 186–190.

7 J. C. Erie, J. A. Good, J. A. Butz and J. S. Pulido, *Am. J. Ophthalmol.*, 2009, **147**, 276–282.

8 P. Hahn, Y. Song, G. S. Ying, X. He, J. Beard and J. L. Dunaief, *Exp. Gerontol.*, 2009, **44**, 594–600.

9 J. C. Erie, J. A. Good and J. A. Butz, *Am. J. Ophthalmol.*, 2009, **148**, 890–894.

10 H. Kobayashi, H. Okamoto, A. Murakami and T. Iwata, *Exp. Anim.*, 2014, **63**, 305–310.

11 http://www.arvo.org/about_arvo/policies/statement_for_the_use_of_animals_in_ophthalmic_and_visual_research/ (accessed on 22nd May 2016).

12 http://www.diamond.ac.uk/Home.html (accessed 22nd May 2016).

13 J. F. W. Mosselmans, A. J. Quinn, A. J. Dent, S. A. Cavill, S. D. Moreno, A. Peach, P. J. Leicester, S. J. Keylock, S. R. Gregory, K. D. Atkinson and J. R. Rosell, *J. Synchrotron Radiat.*, 2009, **16**, 818–824.

14 K. J. S. Sawhney, I. P. Dolbnya, M. K. Tiwari, L. Alianelli, S. M. Scott, G. M. Preece, U. K. Pedersen and R. D. Walton, *AIP Conf. Proc.*, 2010, **1234**, 387.

15 V. A. Solé, E. Papillon, M. Cotte, P. Walter and J. Susini, *Spectrochim. Acta, Part B*, 2007, **62**, 63–68.

16 https://imagej.nih.gov/ij/ (accessed 22nd May 2016).

17 R. Meguro, Y. Asano, S. Odagiri, C. Li, H. Iwatsuki and K. Shoumura, *Arch. Histol. Cytol.*, 2007, **70**, 1–19.

18 J. L. Dunaief, *Invest. Ophthalmol. Visual Sci.*, 2006, **47**, 4660–4664.

19 A. Y. Seo, J. Xu, S. Servais, T. Hofer, E. Marzetti, S. E. Wohlgemuth, M. D. Knutson, H. Y. Chung and C. Leeuwenburgh, *Aging Cell*, 2008, **7**, 706–716.

20 A. M. Daugherty and N. Raz, *Neuropsychol. Rev.*, 2015, **25**, 272–287.

21 M. Schrag, A. Dickson, A. Jiffry, D. Kirsch, H. V. Vinters and W. Kirsch, *BioMetals*, 2010, **23**, 1123–1127.

22 K. Bischoff, C. Lamm, H. N. Erb and J. R. Hillebrandt, *J. Vet. Diagn. Invest.*, 2008, **20**, 220–224.

23 A. B. Lansdown, *Met. Ions Life Sci.*, 2011, **8**, 187–246.

24 D. L. Nickla and J. Wallman, *Prog. Retinal Eye Res.*, 2010, **29**, 144–168.

25 T. Ganz and E. Nemeth, *Nat. Rev. Immunol.*, 2015, **15**, 500–510.

26 M. Theurl, D. Song, E. Clark, J. Sterling, S. Grieco, S. Altamura, B. Galy, M. Hentze, M. U. Muckenthaler and J. L. Dunaief, *FASEB J.*, 2016, **30**, 813–823.

27 N. Wolkow, Y. Song, T. D. Wu, J. Qian, J. L. Guerquin-Kern and J. L. Dunaief, *Arch. Ophthalmol.*, 2011, **129**, 1466–1474.

28 M. Hadzhieva, E. Kirches and C. Mawrin, *Neuropathol. Appl. Neurobiol.*, 2014, **40**, 240–257.

29 M. Zheng, H. Du, W. Ni, L. G. Koch, S. L. Britton, R. F. Keep, G. Xi and Y. Hua, *Transl. Stroke Res.*, 2015, **6**, 215–223.

30 K. R. Chirco, B. A. Tucker, E. M. Stone and R. F. Mullins, *Exp. Eye Res.*, 2015, **146**, 393–397.